

Article

Discovery of Novel EGFR Inhibitor Targeting Wild-Type and Mutant Forms of EGFR: In Silico and In Vitro Study

Duangjai Todsaporn ¹, Alexander Zubenko ², Victor Kartsev ³, Thitinan Aiebchun ⁴, Panupong Mahalapbutr ⁵, Anthi Petrou ⁶, Athina Geronikaki ⁶, Liudmila Divaeva ⁷, Victoria Chekrisheva ², Ilkay Yildiz ⁸, Kiattawee Choowongkamon ^{4,*} and Thanyada Rungrotmongkol ^{1,9,*}

¹ Center of Excellence in Biocatalyst and Sustainable Biotechnology, Department of Biochemistry, Faculty of Science, Chulalongkorn University, Bangkok 10330, Thailand

² North-Caucasian Zonal Research Veterinary Institute, 346406 Novocherkassk, Russia

³ InterBioScreen Ltd., 85355 Moscow, Russia

⁴ Department of Biochemistry, Faculty of Science, Kasetsart University, Bangkok 10900, Thailand

⁵ Department of Biochemistry, Faculty of Medicine, Khon Kaen University, Khon Kaen 40002, Thailand

⁶ Department of Pharmaceutical Chemistry, School of Pharmacy, Aristotle University of Thessaloniki, 54124 Thessaloniki, Greece

⁷ Institute of Physical and Organic Chemistry, Southern Federal University, Pr. Stachki 194/2, 344090 Rostov-on-Don, Russia

⁸ School of Pharmacy, Ankara University, Ankara 06560, Turkey

⁹ Program in Bioinformatics and Computational Biology, Graduate School, Chulalongkorn University, Bangkok 10330, Thailand

* Correspondence: fscikt@ku.ac.th (K.C.); t.rungrotmongkol@gmail.com (T.R.)

Abstract: Targeting L858R/T790M and L858R/T790M/C797S mutant EGFR is a critical challenge in developing EGFR tyrosine kinase inhibitors to overcome drug resistance in non-small cell lung cancer (NSCLC). The discovery of next-generation EGFR tyrosine kinase inhibitors (TKIs) is therefore necessary. To this end, a series of furopyridine derivatives were evaluated for their EGFR-based inhibition and antiproliferative activities using computational and biological approaches. We found that several compounds derived from virtual screening based on a molecular docking and solvated interaction energy (SIE) method showed the potential to suppress wild-type and mutant EGFR. The most promising **PD13** displayed strong inhibitory activity against wild-type (IC_{50} of 11.64 ± 1.30 nM), L858R/T790M (IC_{50} of 10.51 ± 0.71 nM), which are more significant than known drugs. In addition, PD13 revealed a potent cytotoxic effect on A549 and H1975 cell lines with IC_{50} values of 18.09 ± 1.57 and 33.87 ± 0.86 μ M, respectively. The 500-ns MD simulations indicated that **PD13** formed a hydrogen bond with Met793 at the hinge region, thus creating excellent EGFR inhibitory activity. Moreover, the binding of **PD13** in the hinge region of EGFR was the major determining factor in stabilizing the interactions via hydrogen bonds and van der Waals (vdW). Altogether, **PD13** is a promising novel EGFR inhibitor that could be further clinically developed as fourth-generation EGFR-TKIs.

Keywords: furopyridine; molecular dynamics; drug screening; cytotoxicity; EGFR-TK



Citation: Todsaporn, D.; Zubenko, A.; Kartsev, V.; Aiebchun, T.; Mahalapbutr, P.; Petrou, A.; Geronikaki, A.; Divaeva, L.; Chekrisheva, V.; Yildiz, I.; et al. Discovery of Novel EGFR Inhibitor Targeting Wild-Type and Mutant Forms of EGFR: In Silico and In Vitro Study. *Molecules* **2023**, *28*, 3014. <https://doi.org/10.3390/molecules28073014>

Academic Editors: Xin Li and Gregory D. Cuny

Received: 10 February 2023

Revised: 25 March 2023

Accepted: 26 March 2023

Published: 28 March 2023



Copyright: © 2023 by the authors. Licensee MDPI, Basel, Switzerland. This article is an open access article distributed under the terms and conditions of the Creative Commons Attribution (CC BY) license (<https://creativecommons.org/licenses/by/4.0/>).

1. Introduction

EGFR is a transmembrane protein tyrosine kinase that plays an essential role in cellular signaling for cell proliferation, invasion, metastasis, apoptosis, and angiogenesis [1–6]. Structurally, EGFR is composed of three domains—a transmembrane domain, an extracellular domain, and an intracellular tyrosine kinase (TK) domain—which are constructed of four important conserved regions: (i) the activation loop (A-loop), (ii) the glycine-rich loop (G-loop), (iii) the catalytic loop (C-loop), and (iv) the hinge region [7,8]. Deregulation of EGFR is caused by increased EGFR activity such as overexpression and mutations of EGFR [9–11]. Increased EGFR activity is associated with numerous malignant tumors, including esophageal cancers, glioblastoma, anal cancers, epithelial cancers of the head

and neck, breast cancer, and lung cancers [12–16], especially non-small cell lung cancer (NSCLC). Lung cancer is a major cause of cancer death globally, and NSCLC is the most frequently diagnosed cancer [16–18], whereas activating mutations in the tyrosine kinase (TK) domain are recognized as the tumorigenic driver in NSCLC. As a matter of fact, extensive research has been executed to study EGFR function as a therapeutic target for NSCLC.

Several EGFR inhibitors have been developed and reported (Figure 1). Erlotinib [19] and gefitinib [20], first-generation reversible EGFR inhibitors, proved to have a strong response and to lead to prolonged survival in NSCLC patients. However, after 9–14 months of treatment, the secondary “gatekeeper” T790M mutation increased ATP-binding affinity and caused recurrence in most NSCLC patients [21]. Second-generation irreversible EGFR inhibitors targeting EGFR with the T790M activating mutation, such as afatinib [22] and dacomitinib [23], were developed to overcome that problem. Although the irreversible covalent bond with C797 confers enhanced sensitivity and selectivity, serious side effects of these TKIs, such as skin rash and diarrhea due to their activity against wild-type EGFR [22–25], were observed. To combat drug resistance and limit dose-related toxic side effects, Osimertinib (AZD9291), which is a pyrimidine scaffold, was developed as an irreversible third-generation inhibitor [26]. Osimertinib has a high affinity for the drug-resistant L855R/T790M double mutant [27] but no activity against the wild-type EGFR [27–30]. Additionally, clinical studies revealed that approximately 40% of patients who received osimertinib therapy developed a tertiary mutation (C797S) in the EGFR, resulting in a loss of covalent interactions between the irreversible inhibitors and the side chain of C797 [31]. Therefore, the discovery of potent inhibitors of both wild-type and mutant forms of EGFR is required. Since NSCLC is one of oncology’s “big killers” in the patient population and the EGFR signaling is a main driver for this type of tumor, it is a worthwhile endeavor to develop improved therapeutics in the clinical setting.

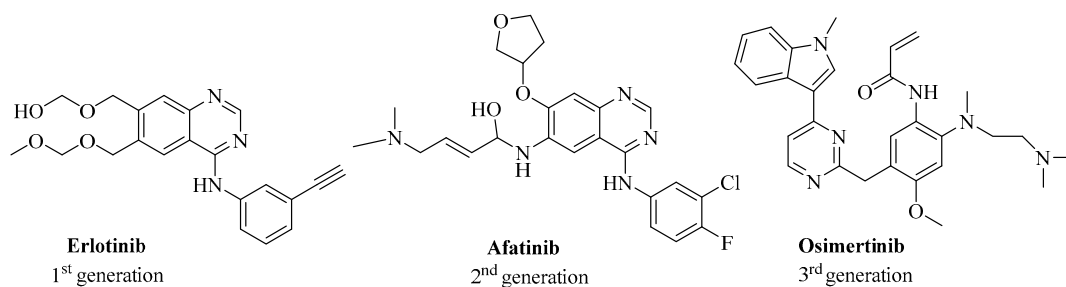


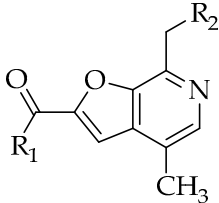
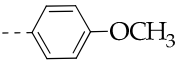
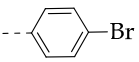
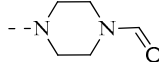
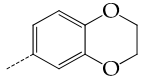
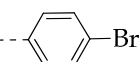
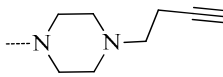
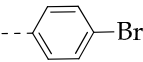
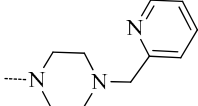
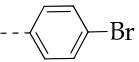
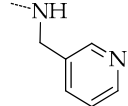
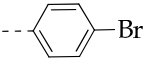
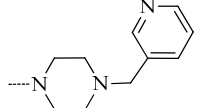
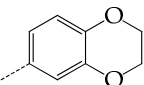
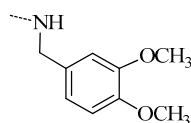
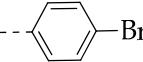
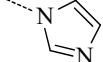
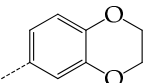
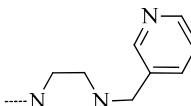
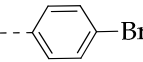
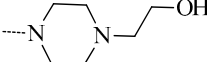
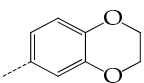
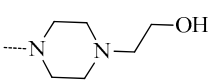
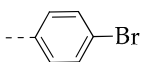
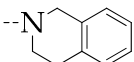
Figure 1. Two-dimensional (2D) structure of three reference drugs targeting EGFR, including erlotinib, afatinib, and osimertinib.

Fuopyridine (PD, Table 1), a furo[2,3-*c*]pyridine compound, is a product of a structural modification of vitamin B₆, which plays an extremely important biological role in living organisms, since it is involved in a wide range of biochemical reactions necessary for cellular metabolism and function. The latter explains why vitamin B₆ and its derivatives are considered biologically privileged molecules with which to develop new therapeutics.

Furthermore, PDs display a wide range of biological activities, including anticancer [32,33], antiviral [34], anti-inflammatory [35], and HIV protease inhibitory activities [36], and also inhibit α -glucosidase [37]. The products of the furan cyclization of pyridoxal under the action of hetarylamine 2-alkylamino-3-hetarylamine-4-hydroxymethylfuro[2,3-*c*]pyridines have an immunostimulating effect due to their selective activation of Toll-like TLR8 receptors [38]. Even though anticancer activity of PD has been reported, an understanding of the binding modes of action of PD and its derivatives against NSCLC remains elusive. Hung et al. [33] reported the antiproliferative activity of synthesized thienopyridine derivatives using the panel of NCI-60 cell lines with GI₅₀ values in the low nanomolarity range, especially the melanoma cell line MDA-MD-435 (GI₅₀—23 nM). Rahman et al. also evaluated the CDK2 inhibitory and antiproliferative activity of pyrazolopyridine, fuopyridine, and pyridine derivatives. Fuopyridine derivative (14) showed IC₅₀ 0.93 μ M as a CDK2

inhibitor as well as significant inhibition on different human cancer cell lines (HCT-116, MCF-7, HepG2, and A549).

Table 1. Chemical structure of fuopyridine; **PD** and its derivatives.

<div style="text-align: center;">  <p>Fuopyridine (PD)</p> </div>					
Cipher	R ₁	R ₂	Cipher	R ₁	R ₂
PD1		OH	PD9		
PD2		OH	PD10		
PD3			PD11		
PD4			PD12		
PD5			PD13		
PD6			PD14		
PD8					

The main aim of this work was the synthesis and evaluation of novel classes of anti-EGFR agents in order to understand the mechanism of anticancer activity as well as their binding modes to the receptor. Herein, we have reported the synthesis of a number of novel fuopyridine derivatives with pharmacologically relevant substituents and also used molecular docking and molecular dynamics (MD) simulations with free energy calculations to virtually screen 14 in-house PD compounds towards wild-type, L858R/T790M, and L858R/T790M/C797S EGFR. Moreover, in vitro EGFR inhibitory and anti-cancer activities against NSCLC cell lines in comparison with normal cell lines were studied. Subsequently, 500-ns MD simulations were carried out to investigate the binding behavior of the most promising PD against wild-type and mutant forms of EGFR. The most promising PD from this work could be further developed as a novel anticancer drug by targeting both wild-type and mutant forms of EGFR.

2. Results

2.1. Virtual Screening

To assess the potency of EGFR inhibitor(s) against wild-type, L858R/T790M, and L858R/T790M/C797S EGFR, molecular docking was carried out on 14 **PD** compounds.

Three drugs—erlotinib, afatinib, and Osimertinib—were selected as a positive control for wild-type, L858R/T790M, and L858R/T790M/C797S EGFR, respectively. The GOLD docking results were plotted in Figure 2. We found that nine PD compounds, including PD3, PD4, PD6, PD8, and PD10–PD13, showed a higher fitness score than erlotinib. Moreover, those PDs were found to inhibit L858R/T790M double mutant EGFR. Interestingly, a series of four PDs (PD4, PD8, PD13, and PD14) exhibited a strong affinity with L858R/T790M/C797S, which is better than osimertinib. The first-round screening suggested that several PD derivatives could be effective in inhibiting both wild-type and mutant forms of EGFR.

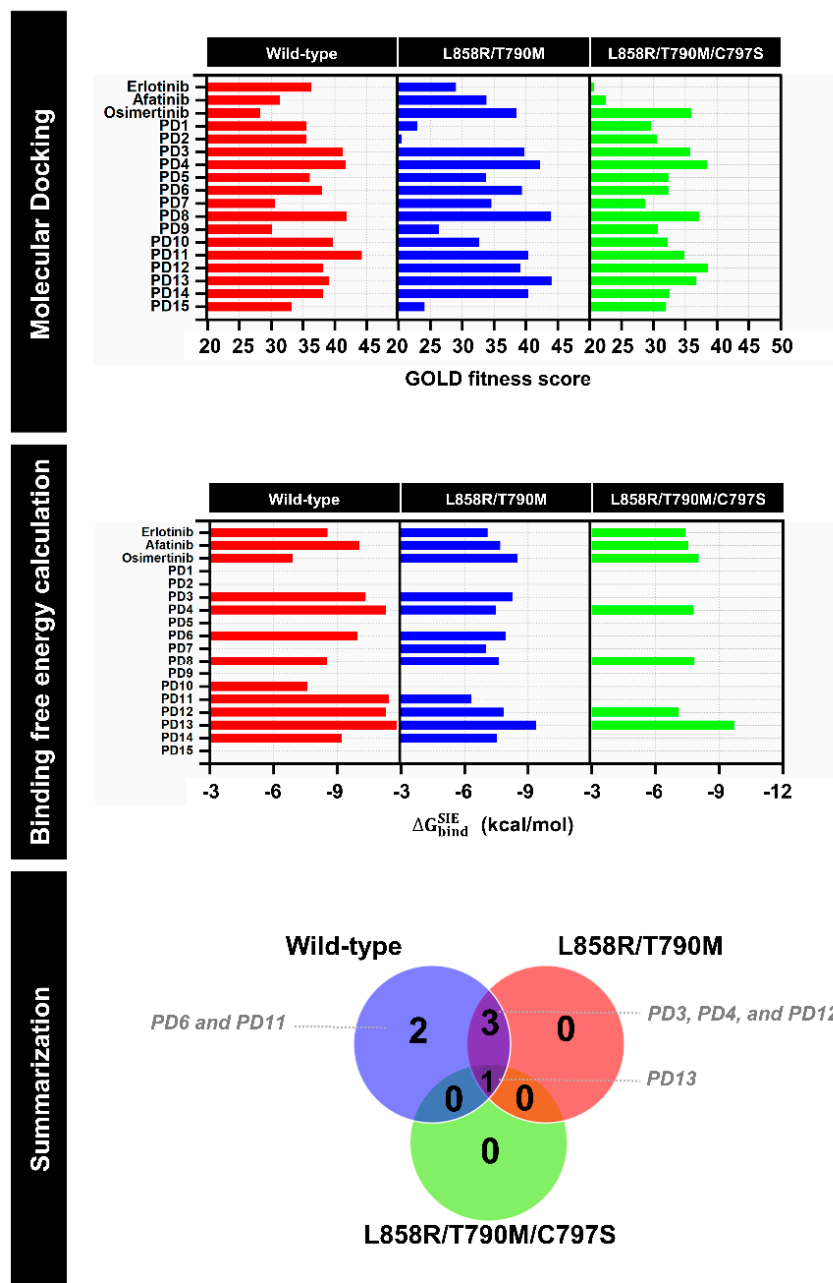
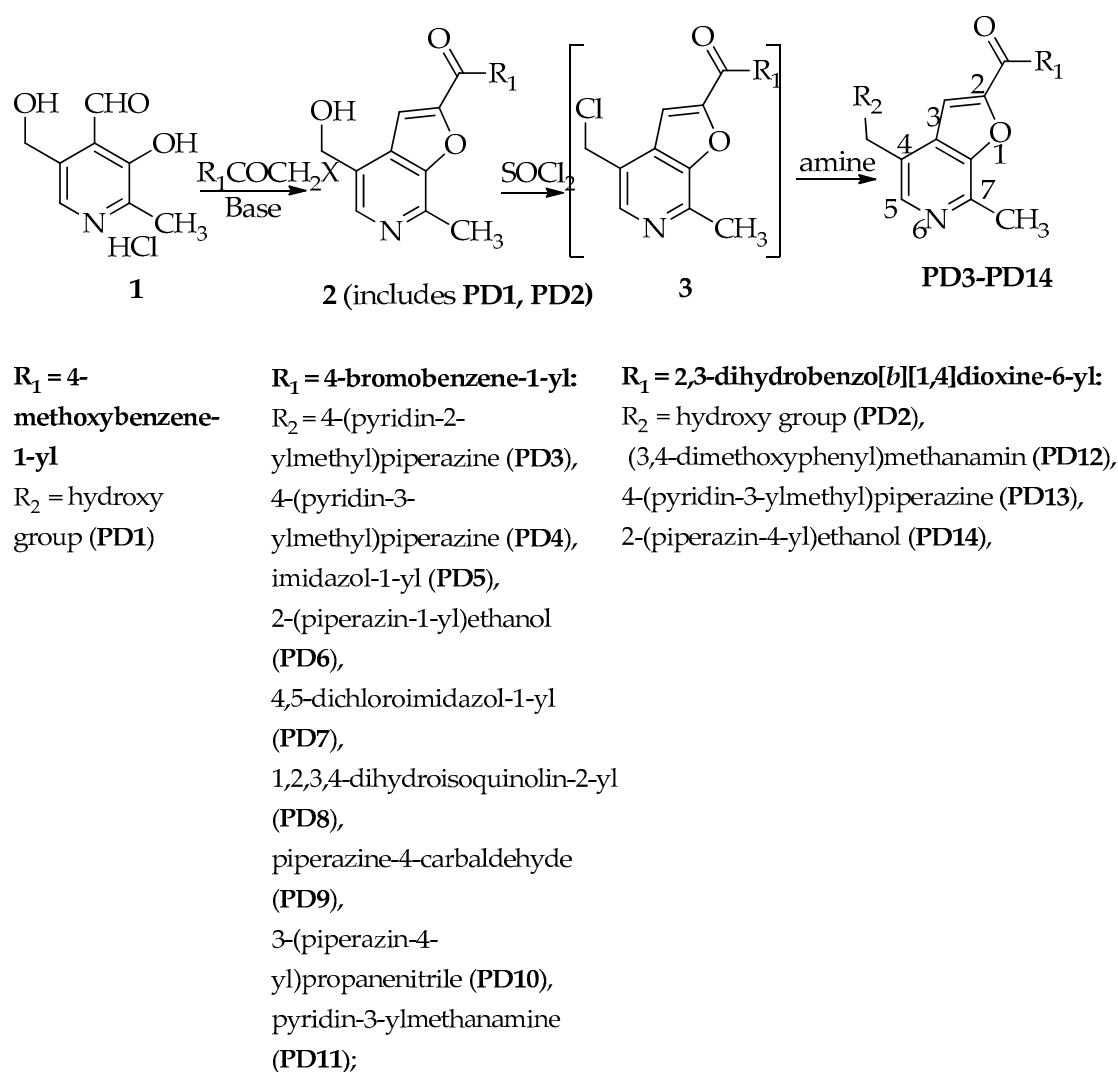


Figure 2. Docking results (top), estimated binding free energy calculation based on SIE method (middle), and summarization of virtual screening (bottom) of furopyridine (PD) derivatives towards wild-type, L858R/T790M, L858R/T790M/C797S EGFR relative to three reference drugs (erlotinib, afatinib, and osimertinib).

To verify the first-round screening, the screened **PDs**/EGFRs complexes derived from molecular docking were subsequently studied on 100 snapshots extracted from the last 10 ns of 100-ns molecular dynamics (MD) simulations. The predicted binding affinity based on the solvated interaction energy (SIE) method of screened **PD** compounds and three positive controls (erlotinib, afatinib, and osimertinib) is shown in Figure 2. **PD6** (ΔG_{bind} of -9.96 kcal/mol) and **PD11** (-11.30 kcal/mol) displayed greater binding affinity than erlotinib (-8.50 kcal/mol) in the wild-type EGFR system, suggesting that both **PD6** and **PD11** were specific for the wild-type EGFR. Moreover, the three **PDs** (**PD3**, **PD4**, and **PD12**) exhibited the most efficient binding to both wild-type and L858R/T790M EGFR, whereas that against L858R/T790M/C797S EGFR showed poor binding affinities. Surprisingly, the most promising, **PD13**, could be able to suppress both wild-type and mutant EGFR. The ΔG_{bind} calculations of **PD13** based on the SIE method gave ΔG_{bind} of wild-type, L858R/T790M, and L858R/T790M/C797S EGFR as follows: -11.81 , -9.39 and -9.7 kcal/mol. Hence, the screened compounds with estimated binding free energies based on the SIE method that were higher than those of the positive controls from each strain of EGFR were synthesized and chosen for in vitro evaluation.

2.2. Chemistry

All the target compounds were synthesized as outlined in Scheme 1.



Scheme 1. Synthesis of target compounds.

The cyclization of pyridoxal hydrochloride **1** in aqueous acetonitrile at 50–60 °C used potassium carbonate as a catalyst soft base, and proceeded fairly quickly in all cases—within 2–3 h—and led to the synthesis of 4-hydroxymethyl-7-methylfuro[2,3-*c*]pyridines (**PD1**, **PD2**). The yields of compounds **PD1**, **PD2** were 55% and 79%, respectively.

The replacement of a hydroxyl group by a chlorine atom in compounds **PD1**, **PD2**, by the action of thionyl chloride in DMF furnished the target compounds **2** [39]. Further, the reaction of the resulting chloromethyl derivatives **3** with alkyl- and dialkylamines resulted in the formation of the corresponding 4-aminomethylfuro[2,3-*c*]pyridines **PD3–PD14**. It was more convenient to carry out the reactions in EtOH (for **PD3–PD6**, **PD9–PD11**, 25 °C—reflux, 3–6 h) or DMF (for **PD7**, **PD8**, **PD12**, **PD13**, 30–40 °C, 3–5 h).

The R₁ and R₂ substituents were chosen considering that the biological activity of the compounds, as well as their pharmacodynamics and pharmacokinetics, are significantly affected by both electronic factors (electron donation or electron acceptor of substituents) and their physical properties (lipophilicity, hydrophilicity, polarizability, etc.)

The structure of the obtained furo[2,3-*c*]pyridines was confirmed by ¹H NMR spectroscopy. ¹H NMR data for compounds **PD1**, **PD2** can be illustrated by the example of 4-hydroxymethylfuro[2,3-*c*]pyridines **PD1**. The ¹H NMR of this ketone showed the proton signals of H-3 and H-5 of the bicyclic system (singlets at 7.79 and 8.24 ppm, respectively), the benzoyl group (two-proton, somewhat distorted doublet at 8.10 ppm (H-2', H-6', *J* 8.7 Hz) as well as multiplet at 7.08–7.14 (2H, H-3', H-5')), the hydroxymethyl group (two-proton and single-proton singlets at 4.79 and 5.24 ppm, respectively), and the methyl group (singlet at 2.76 ppm) (see Supplementary Files, ¹H-NMR spectra) (SI).

In the spectra of amino derivatives **PD3–PD14**, there was no signal of the CH₂OH group, while in the hydrochlorides of these compounds (**PD3–PD5**, **PD9**, **PD11–PD14**), a broadened singlet of the NH⁺ group appeared in the region of 5.01–5.71 ppm. The aromatic proton signals of these compounds (**PD3–PD14**) correspond to the proposed structures and differ from the signals of 4-hydroxymethylfuro[2,3-*c*]pyridine (**PD1**) by 0.1–0.3 ppm (see Supplementary Files, ¹H-NMR spectra). The ¹³C-NMR of all these compounds was in agreement with their structure (see Supplementary Materials, ¹³C-NMR).

2.3. Kinase Inhibitory Activities of EGFR

Potent compounds obtained from *in silico* screening were selected to elucidate their inhibitory EGFR activity against different types of EGFR (wild-type, L858R/T790M and L858R/T790M/C797S). Note that erlotinib, afatinib, and osimertinib, which are FDA-approved drugs targeting EGFR, were used as the positive control. The selected compounds and drugs were first screened to observe the sign of EGFR using a single 1 μM dose concentration. The **PD** compounds that present a percentage value of EGFRs inhibition <50 were selected to calculate the IC₅₀ values. The relative inhibition of EGFR and IC₅₀ curves were analyzed and are plotted in Figure 3, and the IC₅₀ values of focused **PD** and drugs are summarized in Table 2. It was found that **PD13** was active in wild-type and L858R/T790M forms of EGFR, whereas **PD4** was only against wild-type EGFR.

The IC₅₀ values of **PD4** and **PD13** were determined in comparison with reference drugs (Table 2). The IC₅₀ values of two **PD** compounds and drugs inhibiting three strains of EGFR were in the nanomolar range. **PD4**/wild-type (IC₅₀ of 4.78 ± 0.73 nM) displayed EGFR inhibitory activity >2-fold compared to erlotinib (of 14.11 ± 0.19 nM). On the other hand, **PD4** complexed with L858R/T790M (91.02 ± 2.01 nM) and L858R/T790M/C797S EGFR (103.70 ± 3.62 nM) gave the IC₅₀ value of >100 nM, suggesting that **PD4** is specific against wild-type EGFR. **PD13** showed the lowest IC₅₀ values for both wild-type (11.64 ± 1.30 nM) and L858R/T790M (10.51 ± 0.71 nM). While **PD13** inhibited L858R/T790M/C797S EGFR with IC₅₀ values in the double-digit nanomolar range, it had lower potencies than third-generation EGFR inhibitor osimertinib. Furthermore, the **PD13**/triple mutant EGFR appeared to be a more promising candidate compound than previously reported L858R/T790M/C797S EGFR inhibitors such as 2,9-disubstituted-8-phenylthio/phenyl-sulfinyl-9H-

purines (IC₅₀ of 114 nM) [40], quinoline derivative (IC₅₀ of 113 nM) [41], or 5-methylpyrimidopyridone derivative (IC₅₀ of 27.5 nM) [42].

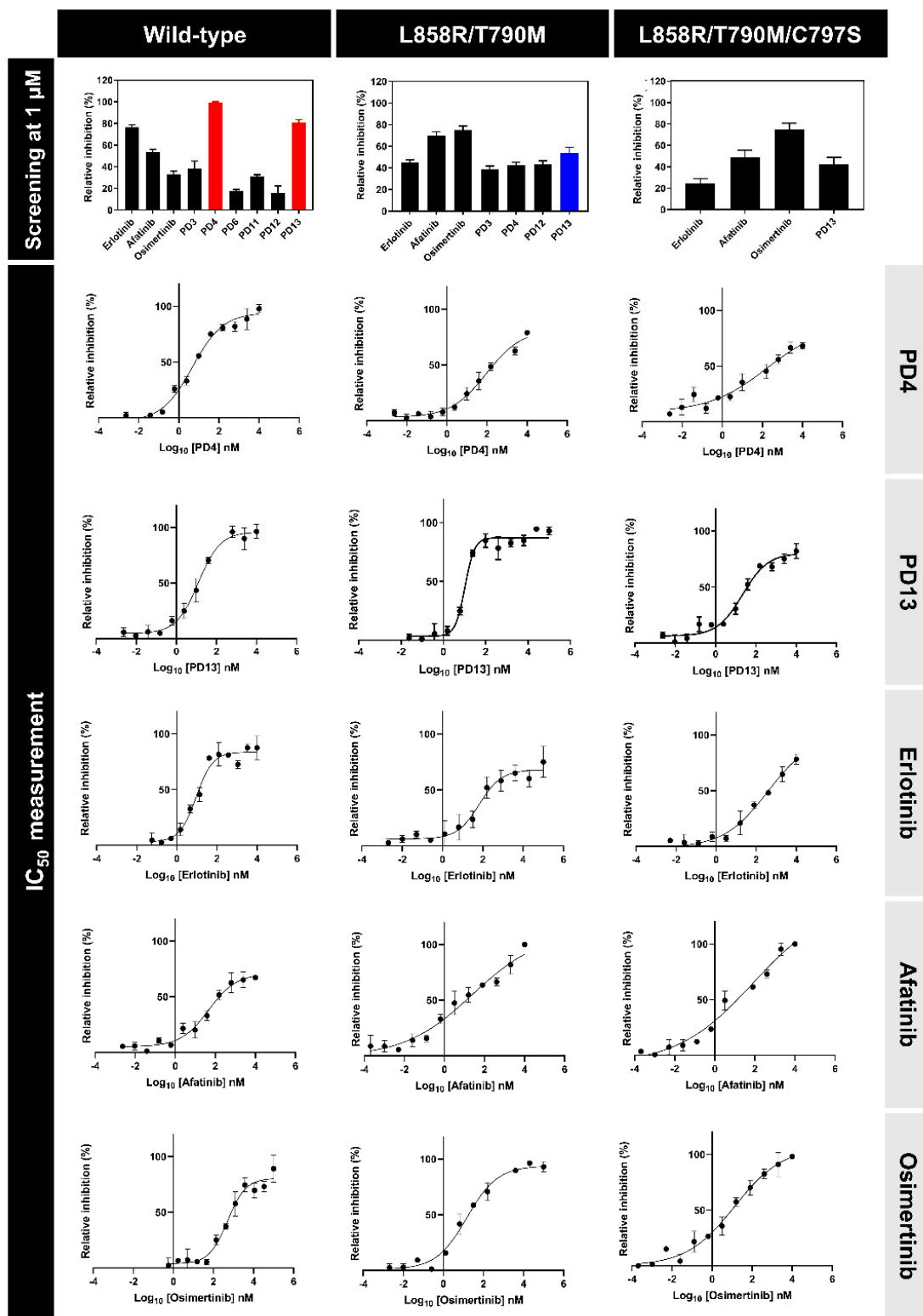


Figure 3. Three forms of EGFR (wild-type, L858R/T790M, and L858R/T790M/C797S) inhibitory screening of PD derivatives at 1 μ M concentration (**top**) and IC₅₀ curves of compounds that present more than 50% PD4 and PD13 in comparison with reference drugs (**bottom**).

Table 2. EGFR inhibitory activities of focused **PD** and drugs in different forms of EGFR.

Compounds	Wild-Type	IC ₅₀ (nM)	
		L858R/T790M	L858R/T790M/C797S
PD4	4.78 ± 0.73	91.02 ± 2.01	103.70 ± 3.62
PD13	11.64 ± 1.30	10.51 ± 0.71	21.93 ± 1.79
Erlotinib	14.11 ± 0.19	87.96 ± 0.89	108.50 ± 1.54
Afatinib	78.19 ± 1.20	20.14 ± 0.58	23.86 ± 2.02
Osimertinib	441.90 ± 3.02	17.39 ± 0.25	8.98 ± 0.53

2.4. Antiproliferative Activities on NSCLC and Normal Cell Lines

The antiproliferative activity of two focused **PD** compounds and drugs were evaluated against NSCLC cell lines, namely the wild-type NSCLC cell line A549 as well as L858R/T790M mutant NSCLC cell line H1975. Erlotinib, afatinib, and osimertinib were used as positive controls. The results are summarized in Table 3. We found that both **PD4** and **PD13** exhibited strong anti-cancer activity by inhibiting the proliferation of A549 rather than H1975 cell lines. In addition, **PD13** exhibited stronger antiproliferative activities than afatinib and osimertinib against the A549 cell line. Moreover, **PD13** showed cell growth inhibition in H1975 cell cultures at a similar level to afatinib.

Table 3. In vitro anticancer activity of focused **PD** and drugs against NSCLC and normal cell lines.

Compounds	A549	IC ₅₀ (μM)	
		H1975	Vero
PD4	19.70 ± 0.59	27.26 ± 1.02	>50
PD13	18.09 ± 1.57	33.87 ± 0.86	>100
Erlotinib	19.43 ± 0.79	41.84 ± 2.19	>30
Afatinib	34.69 ± 0.67	27.33 ± 1.87	>50
Osimertinib	25.28 ± 1.21	18.33 ± 2.00	>50

Furthermore, **PD4**, **PD13**, and positive controls were then investigated for their cytotoxicity to the normal cell line Vero (monkey kidney epithelial cells). We found that the IC₅₀ value of **PD13** was >100 μM in Vero cells, whereas for **PD4** IC₅₀ was <100 μM. These results suggested that **PD13** showed low cytotoxicity against the normal cell. Therefore, **PD13** was chosen in order to study its binding affinity by MD simulations.

2.5. System Stability

The stability of **PD13** and the reference drugs erlotinib, afatinib, and osimertinib was determined using all-atom root mean square displacement (RMSD) to observe the system stability. The RMSD values of each system were obtained from three independent simulations. As shown in Figure 4, the RMSD values of the erlotinib system dramatically increased in the first 100 ns and were maintained at the fluctuation of ~2.0–3.0 Å until the end of the simulation for all independent runs. The wild-type/**PD13** complexes reached three runs after 300 ns. The RMSD values of afatinib complexed with L858R/T790M EGFR fluctuated ~1.5–3.0 Å and were maintained at the fluctuation of ~2.0–3.0 Å until the end of the simulation. In the case of **PD13**/double mutant, EGFR showed similar patterns to the three independent simulations. The RMSD value of osimertinib continuously increased in the first 100 ns and was stably maintained at a fluctuation of 3.0–4.0 Å. L858R/T790M/C797S complexed with **PD13** appeared to be quite stable after 400 ns for all simulated systems, while the RMSD value of **PD13** and known drugs complexed with EGFRs of all systems tended to be stable after 200 ns. Altogether, the MD trajectories from 400 to 500 ns of each simulation were extracted for further analysis in terms of: (i) key binding residues; (ii) protein-ligand hydrogen bonding; and (iii) binding affinity.

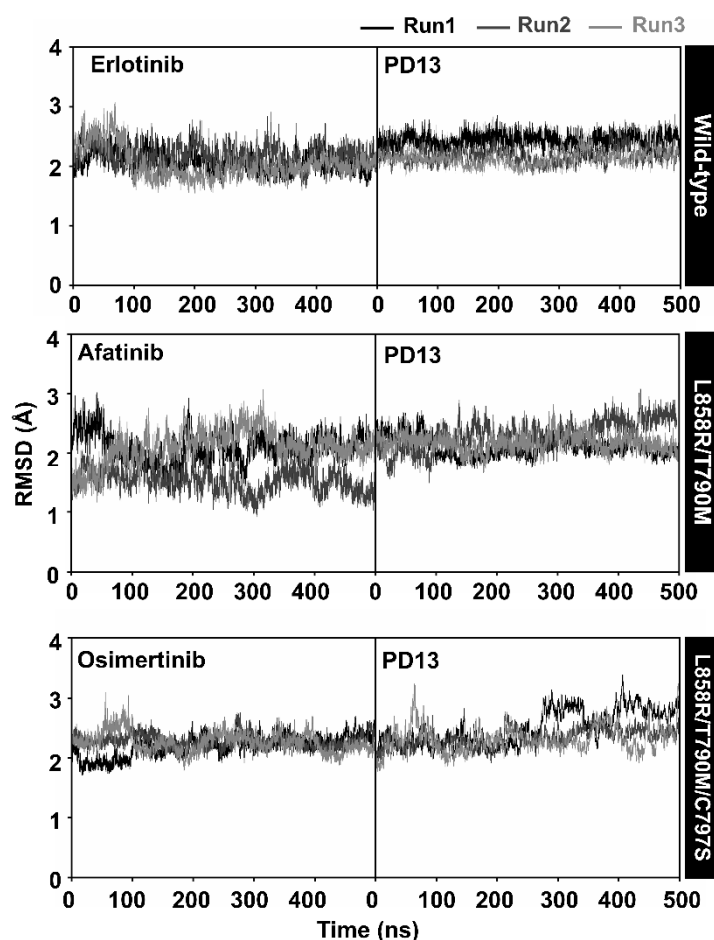


Figure 4. All-atom RMSD of EGFRs with PD13 and drugs during 500 ns of simulation from three independent simulations.

2.6. Key Binding Residues

To explore the binding affinity of PD13 and reference drugs, the per-residue free energy decomposition ($\Delta G_{\text{bind}}^{\text{residue}}$) based on the MM/PBSA method was calculated on 100 snapshots extracted from the last 100 ns of all simulations. Note that, among the 695–1018 residues of EGFR, only the energy stabilization of ≤ -1.0 kcal/mol for the 700–900 residues of all systems was plotted in Figure 5. The compounds were shaded based on their highest and lowest energies, with white representing the highest energies and blue representing the lowest energies.

The wild-type/erlotinib showed important residue for binding ten residues including L718, V726, A743, K745, T790, L792, M793, G796, C797, and L844. Interestingly, the PD13/wild-type complex displayed a similar binding pattern to that of reported EGFR inhibitors and was stabilized by L718 (-3.74 kcal/mol, dark red) at the hinge region, which is in good agreement with a previous study that identified L718, A743, L792, M793, G796, and L844 as key residues involved in the main binding of EGFR inhibitors [43–45]. In addition, the residue M793 of L858R/T790M EGFR exhibited the highest stabilization for PD13 (-3.43 kcal/mol, dark red) compared to the afatinib (-3.21 kcal/mol, red) system. This may be one of the reasons that explains why PD13 could inhibit L858R/T790M EGFR better than afatinib. The binding of PD13 with L858R/T790M/C797S EGFR displayed a higher number of amino acid residues than Osimertinib; L718, V726, A743, K745, M766, L788, M790, L792, M793, G796, S797, and L844 are all involved in ligand stabilization. Among all the residues, the moderate L858R/T790M/C797S EGFR inhibitory potency of PD13 may be due to steric clashing of M790 with the phenyl ring of the inhibitor.

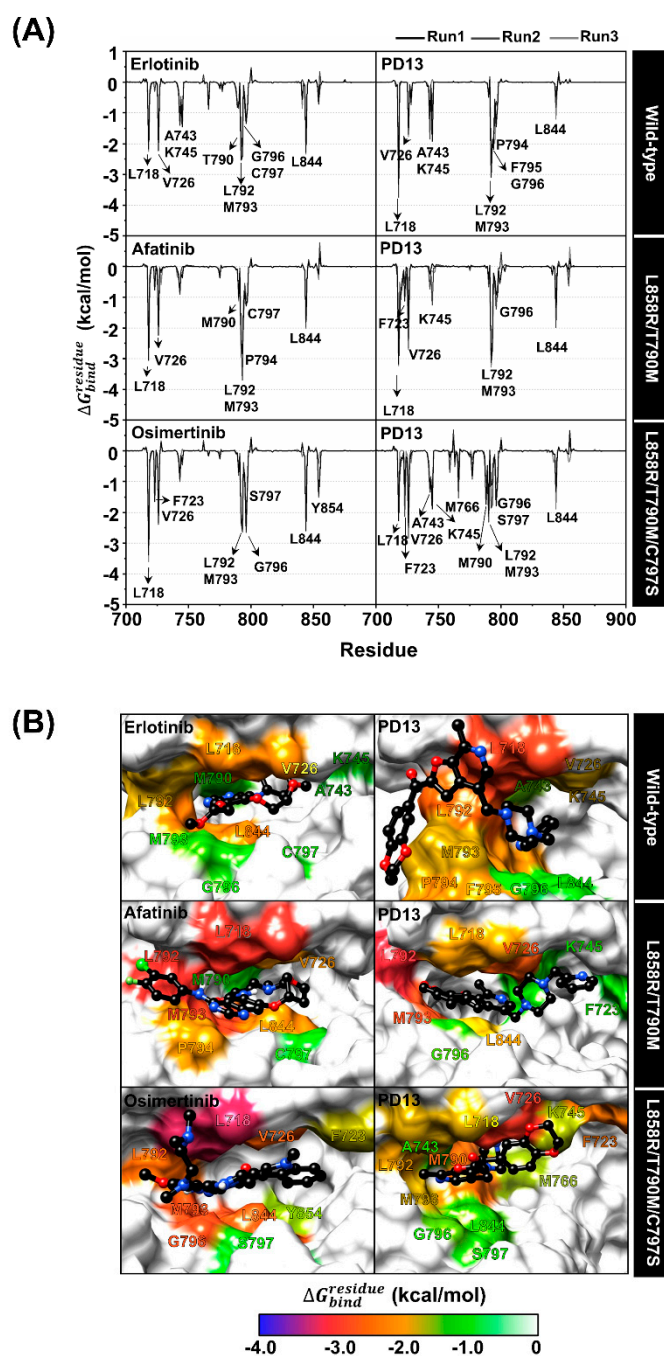


Figure 5. (A) Per-residue decomposition free energy of EGFRs for the binding of PD13 and drugs from three independent simulations (**top**). (B) The binding orientation of PD13 and drugs within the binding pocket of EGFR was drawn from the last snapshot. The lowest and highest energies are shaded from blue to white (**bottom**).

2.7. Protein-Ligand Hydrogen Bonding

The hydrogen bond is one of the main factors for determining the binding strength of the protein–ligand complex. We further calculated the hydrogen bond occupations between EGFRs with PD13 and reference drugs using the two following criteria: (i) distance between hydrogen donor (HD) and acceptor (HA) ≤ 3.5 Å; and (ii) the angle between HD and HA being over 120° ($\text{HD}-\text{H} \cdots \text{HA} \geq 120^\circ$). The percentages of hydrogen bond occupations for the studied ligands were observed and are compared in Figure 6.

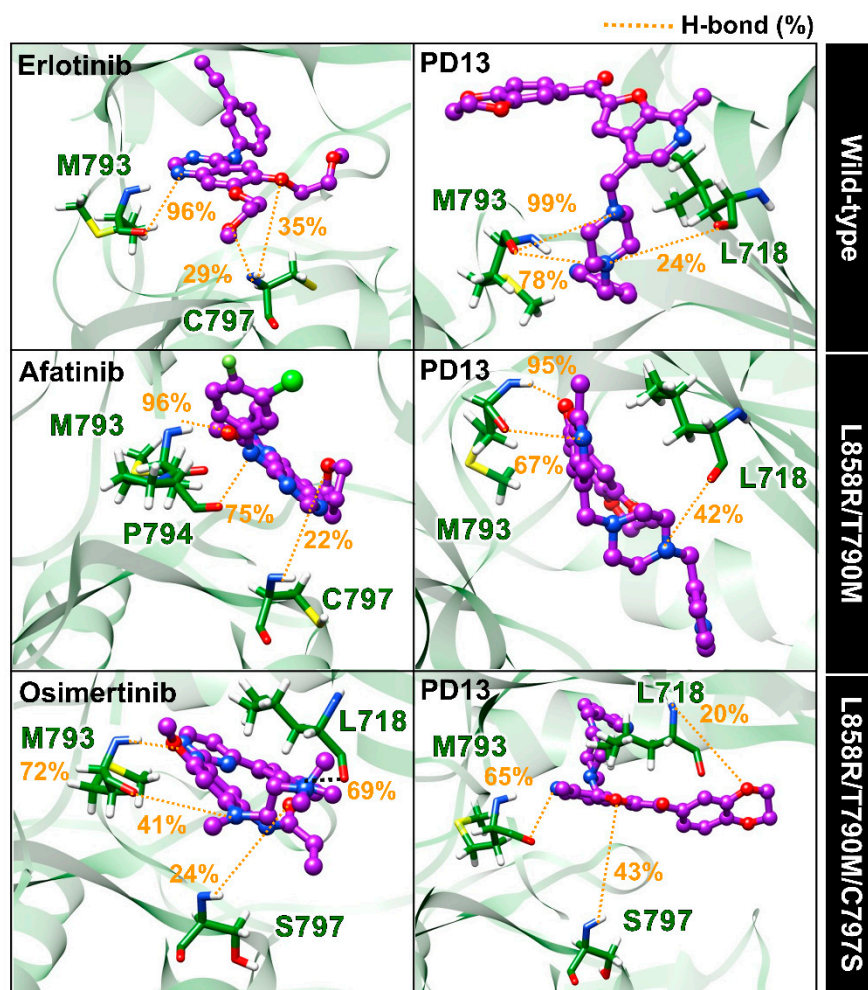


Figure 6. The three-dimensional representative structures showing a percentage of the H-bond occupations of PD13 and drugs with EGFRs, drawn from the last snapshot of run1. The yellow dashed lines indicate H-bond formation.

The hydrogen bond formations of wild-type/PD13 indicated strong stabilization with the M793 (78–98%) and L718 (24%), and are similar to that found in wild-type/erlotinib complex. In the case of L858R/T790M double EGFR, this compound formed a hydrogen bond with M793 (67–95%) and L718 (42%), in good agreement with the per-residue decomposition analysis mentioned above. PD13 complexed with triple mutant EGFR showed similar H-bond formations to those of other forms of EGFR (except S797). We speculate that S797 residue that is mutated EGFR could lead to moderate inhibitory activity of L858R/T790M/C797S EGFR due to more favorable interactions with S797 via a hydrogen bond. Therefore, the inhibitory activity of PD13/EGFRs was induced by the two key residues, which are M793 and S797, at the hinge region. The main EGFR residues (L718, M793, and S797) evidenced crucial binding via hydrogen bonds, which is similar to other reported EGFR tyrosine kinases such as tupichinol E [46], quinazoline [47], and 9-heterocyclyl substituted 9H-purine derivatives [48].

2.8. Binding Affinity

The binding efficiency of PD13 and reference drugs was calculated using the MM/PBSA approach on 100 snapshots extracted from the last 100 ns of three independent simulations. The values of the averaged ΔG_{bind} over the three independent simulations are listed in Table 4 in comparison with the half-maximal inhibitory concentration (IC_{50}).

Table 4. The average ΔG_{bind} and its energy component (kcal/mol) of **PD13** and drugs in complexes with EGFRs calculated with the MM/PBSA method, compared to the half-maximal inhibitory concentration (IC_{50}) values. Data are shown as mean \pm standard deviation (SD) of three independent simulations.

	ΔE_{ele}	ΔE_{vdW}	ΔE_{MM}	TAS	ΔG_{sol} (PBSA)	ΔG_{bind} (PBSA)	IC_{50} (nM)	$\Delta G_{\text{bind,exp}}$
Wild-type								
Erlotinib	-15.43 ± 1.02	-65.54 ± 1.52	-80.98 ± 1.87	-22.69 ± 0.94	45.70 ± 0.96	-12.57 ± 0.69	11.44	10.83
PD13	-25.46 ± 2.01	-98.54 ± 0.89	-124.01 ± 0.71	-27.98 ± 0.75	77.69 ± 0.05	-18.33 ± 0.42	14.11	10.70
L858R/T790M/58								
Afatinib	-15.56 ± 0.85	-60.87 ± 0.66	-79.44 ± 0.09	-20.47 ± 0.99	39.23 ± 0.12	-19.73 ± 0.95	20.14	10.49
PD13	-14.36 ± 0.83	-91.64 ± 1.99	-106.00 ± 3.54	-10.21 ± 0.87	73.11 ± 0.93	-22.68 ± 0.47	10.51	10.88
L858R/T790M/C797S								
Osimertinib	-20.03 ± 0.79	-61.65 ± 1.20	-81.68 ± 0.28	-19.24 ± 0.88	42.57 ± 0.45	-19.87 ± 0.84	8.98	10.97
PD13	-12.02 ± 1.44	-94.02 ± 0.98	-106.04 ± 0.95	-18.21 ± 1.55	71.11 ± 0.69	-16.71 ± 0.69	21.93	10.44

In the gas term, we found that vdW interactions were three- to fourfold higher than electrostatic interactions in all studied ligands. Therefore, vdW interactions play an important role in the recognition of **PD13** and reference drugs. These interaction findings are strongly consistent with previous studies on several small-molecule therapeutic kinase inhibitors such as olmutinib, lapatinib, and icotinib [49–51]. From the ΔG_{bind} calculation, the predicted binding values produced similar phenomena to that of experimental ΔG_{bind} values converted from the IC_{50} values, indicating that the MM/PBSA approach produced reliable ΔG_{bind} results. It was found that **PD13** complexed with the wild-type and L858R/T790M system had a better binding affinity than erlotinib or afatinib, respectively. While **PD13** complexed with L858R/T790M/C797S displayed lower binding affinity than osimertinib, the results agree well with in vitro L858R/T790M/C797S EGFR inhibitory activities, showing that this compound could inhibit wild-type and L858R/T790M better than L858R/T790M/C797S EGFR.

3. Materials and Methods

3.1. General Information

NMR ^1H (300 MHz) and ^{13}C (125 MHz) spectra of newly synthesized compounds were recorded on a spectrometer Bruker AC-300 (300 MHz) and BRUKER AVANCE NEO 500 MHz FT spectrometers in DMSO- d_6 . Chemical shifts of nuclei ^1H were measured relative to the residual signals of deuteriosolvent ($\delta = 2.50$ ppm). Coupling constants (J) are reported in Hz. Melting points were determined by using Fisher-Johns Melting Point Apparatus (Fisher Scientific) and are uncorrected. Elemental analysis was performed using the classical method of microanalysis. The reaction and purity of the obtained compounds were monitored by TLC (plates with Al_2O_3 III activity grade, eluent CHCl_3 , development of TLC plates by exposition to iodine vapors in “iodine chamber”).

3.2. Chemistry

The reaction conditions and yields of compounds **PD3–PD14** are presented in Table 5. Compound **PD2** was synthesized as described previously [39].

[4-Hydroxymethyl-7-methylfuro[2,3-*c*]pyridin-2-yl](4-methoxyphenyl)methanone (**PD1**).

The mixture of pyridoxal hydrochloride **1** (1.02 g, 0.05 mol) and 2-bromo-1-(4-methoxyphenyl)ethan-1-one (1.0 g, 0.05 mol) with a saturated aqueous solution of K_2CO_3 (10 mL), CH_3CN (10 mL) and 0.05 g TEBA was stirred vigorously at 20–25 °C for 1 h and at 50–60 °C for 3 h. The mixture was cooled, water (50 mL) was added, and the formed precipitate was filtered off and washed with water (15 mL). Yield: 0.76 g (57%). Light beige crystals, m.p. 147–148 °C (CH_3CN). ^1H NMR (DMSO- d_6 : δ ppm 2.76 (s, 3H, Me), 3.93 (s, 3H, OCH_3), 4.79 (s, 2H, CH_2), 5.24 (br. s, 1H, OH), 7.08–7.14 (m, 2H, H-3', H-5'), 7.79 (s, 1H, H-3), 8.10 (d, 2H, J 8.7, H-2', H-6'), 8.24 (s, 1H, H-5)). ^{13}C NMR (DMSO- d_6) δ ppm: 18.322, 55.607, 58.928, 113.455, 114.154, 128.664, 129.946, 130.748, 131.870, 139.910, 142.353, 150.118, 152.76, 163.576,

181.882 (DMSO-*d*₆: 38.795–40.045). Anal.Calc. for C₁₇H₁₅NO₄: (%). C, 68.68; H, 5.09; N, 4.71%. Found: C, 68.53; H, 5.00; N, 4.67%.

Table 5. Reaction conditions and yields of compounds **PD3–PD14**.

Furopyridine	Solvent (mL)	Reagent R ₃ NH (mmol)	Reaction Temperature (°C)	Reaction Time (h)	Yield (%)
PD3	EtOH 10	3	25–30	6.0	62
PD4	EtOH 10	3	25–30	6.0	66
PD5	EtOH 10	12	boiling	3.0	47
PD6	EtOH 10	10	25–30	6.0	73
PD7 ¹	DMF 8	3	35–40	3.0	93
PD8	DMF 10	3	45–50	6.0	75
PD9	EtOH 8, H ₂ O 2	3	boiling	3.0	68
PD10	EtOH 10	3	40–45	5.0	84
PD11	EtOH 10	3	35–40	5.0	44
PD12	DMF 5	3	30–40	5.0	61
PD13 ²	DMF 5	3.5	30–40	5.0	58
PD14 ²	DMF 5	3.5	30–40	5.0	75

Note: 1. For compound synthesis, **PD7** NaH (3.5 mmol) was used instead of K₂CO₃. 2. For compounds synthesis, **PD13**, **PD14** NaHCO₃ (6 mmol) was used instead of K₂CO₃.

General Procedure for the Synthesis of 7-Methylfuro[2,3-*c*]pyridine Derivatives **PD3–PD14**

A mixture of corresponding 4-chloromethyl derivative **3** (3 mmol) [41], saturated K₂CO₃ solution (3 mL) and corresponding amine (3 mmol) in solvent was stirred. Conditions for the reaction are given in Table 1. Then, 50 mL of water was added, and the formed precipitate was filtered off and washed with water (15 mL). To convert the amines **PD3–PD5**, **PD9**, and **PD11–PD14** into their hydrochlorides, they were treated with a saturated solution of HCl in isopropanol until a weakly acidic reaction occurred (pH~3).

(4-Bromophenyl){7-methyl-4-[(4-(pyridin-2-ylmethyl)piperazin-1-yl)methyl]furo[2,3-*c*]pyridin-2-yl)methanone dihydrochloride (**PD3**).

Yield: 1.08 g (62%). Light beige crystals, m.p. 224–225 °C (EtOH). ¹H NMR (DMSO-*d*₆): δ ppm 2.98 (s, 3H, CH₃), 3.48 (s, 4H, H-3', H-5'), 3.60 (s, 4H, H-2', H-6'), 4.45 (s, 2H, CH₂), 4.84 (s, 2H, CH₂), 6.54 (br. s, 2H, 2NH⁺), 7.59–7.65 (m, 1H, H-3), 7.79–7.82 (m, 2H, H-3''', H-5'''), 7.91 (t, *J* 7.8, 1H, H-4'''), 8.11–8.15 (m, 3H, H-2'', H-6'', H-6'''), 8.60 (s, 1H, H-3''), 8.70–7.72 (m, H-5''), 8.85 (s, 1H, H-5). ¹³C NMR (DMSO-*d*₆) δ ppm: 15.936, 47.989, 52.125, 57.351, 115.179, 125.002, 126.285, 128.292, 131.703, 132.094, 134.511, 137.749, 140.949, 143.629, 146.405, 149.727, 150.445, 155.023, 182.261 (DMSO-*d*₆: 38.872–40.128) Anal.Calc. for C₂₆H₂₇BrCl₂N₄O₂: (%): C, 54.00; H, 4.71; Br, 13.82; Cl, 12.26; N, 9.69%. Found: C, 54.11; H, 4.62; Br+Cl, 26.21; N, 9.57%.

(4-Bromophenyl){7-methyl-4-[(4-(pyridin-3-ylmethyl)piperazin-1-yl)methyl]furo[2,3-*c*]pyridin-2-yl)methanone dihydrochloride (**PD4**).

Yield: 1.15 g (66%). Light beige crystals, m.p. 243–247 °C (EtOH). ¹H NMR (DMSO-*d*₆): δ ppm 2.96 (s, 3H, CH₃), 3.47–4.54 (m, 8H, H-2', H-3', H-5', H-6'), 4.50 (s, 2H, CH₂), 4.77

(s, 2H, CH₂), 5.01 (br. s, 2H, 2NH⁺), 7.09 (s, 1H, H-3), 7.81 (d, *J* 8.3, 2H, H-2'', H-6''), 7.94 (s, 1H, H-5'''), 8.13 (d, *J* 8.6, 2H, H-3'', H-5''), 8.53 (s, 1H, H-6'''), 8.76–8.86 (m, 2H, H-5, H-2'''), 9.13 (s, 1H, H-4'''). ¹³C NMR (75 MHz, DMSO-*d*₆) δ 183.53 (C=O), 154.28 (C-O), 149.52, 149.14, 148.43, 144.52, 143.19, 135.46, 135.30, 132.46, 131.94 (2C), 131.70 (2C), 131.41, 126.45, 124.62, 123.68, 108.85, 61.71, 58.29, 52.21 (2C), 49.11 (2C), 18.49 (CH₃). Anal. Calc for C₂₆H₂₇BrCl₂N₄O₂ (%): C, 54.00; H, 4.71; Br, 13.82; Cl, 12.26; N, 9.69%. Found: C, 54.06; H, 4.64; Br+Cl, 26.11; N, 9.57%.

{4-[(1H-imidazol-1-yl)methyl]-7-methylfuro[2,3-*c*]pyridin-2-yl}(4-bromophenyl)methanone hydrochloride (PD5).

Yield: 0.61 g (47%). Light beige crystals, m.p. 278–280 °C (EtOH). ¹H NMR (DMSO-*d*₆): δ ppm 2.87 (s, 3H, CH₃), 5.89 (s, 2H, CH₂), 7.10 (s, 1H, H-3), 7.60 (s, 1H, H-4'), 7.82 (d, *J* 8.4, 2H, H-3'', H-5''), 7.89 (s, 1H, NH⁺), 8.04 (d, *J* 8.5, 2H, H-2'', H-6''), 8.39 (s, 1H, H-5'), 8.72 (s, 1H, H-2'), 9.60 (s, 1H, H-5). ¹³C NMR (DMSO-*d*₆) δ ppm: 16.267, 46.364, 113.426, 120.075, 120.736, 121.986, 124.275, 128.174, 131.565, 131.976, 134.457, 135.624, 138.606, 143.633, 149.820, 155.206, 182.194 (DMSO-*d*₆: 38.831–40.082). Anal. Calc for C₁₉H₁₅BrClN₃O₂ (%): C, 52.74; H, 3.49; Br, 18.47; Cl, 8.19; N, 9.71%. Found: C, 52.81; H, 3.29; Br+Cl, 26.80; N, 9.64%.

(4-Bromophenyl){4-[(4-(2-hydroxyethyl)piperazin-1-yl)methyl]-7-methylfuro[2,3-*c*]pyridin-2-yl)methanone (PD6).

Yield: 1.00 g (73%). Light beige crystals, m.p. 105–107 °C (EtOH). ¹H NMR (DMSO-*d*₆): δ ppm 2.54 (s, 8H, H-2', H-3', H-5', H-6'), 2.75 (s, 6H, CH₃, CH₂, OH), 3.54 (s, 2H, CH₂), 3.79 (s, 2H, CH₂), 7.77–7.82 (m, 2H, H-3'', H-5''), 7.87 (s, 1H, H-3), 7.98–8.03 (m, 2H, H-2'', H-6''), 8.23 (s, 1H, H-5). ¹³C NMR (DMSO-*d*₆) δ ppm: 16.667, 47.502, 52.632, 115.417, 128.247, 131.716, 132.107, 134.697, 136.832, 141.641, 144.212, 149.804, 154.369, 161.108, 182.485 (DMSO-*d*₆: 38.872–40.122). Anal. Calc for C₂₂H₂₄BrN₃O₃ (%): C, 57.65; H, 5.28; Br, 17.43; N, 9.17%. Found: C, 57.58; H, 5.11; Br, 17.80; N, 9.04%.

(4-Bromophenyl){4-[(4,5-dichloro-1H-imidazol-1-yl)methyl]-7-methylfuro[2,3-*c*]pyridin-2-yl)methanone (PD7).

Yield: 1.30 g (93%). Light beige crystals, m.p. 183–185 °C (EtOAc: CH₃CN 1:1). ¹H NMR (DMSO-*d*₆): δ ppm 2.77 (s, 3H, CH₃), 5.56 (s, 2H, CH₂), 7.78–7.82 (m, 2H, H-2'', H-6''), 7.91 (s, 1H, H-3), 7.98–8.01 (m, 2H, H-3'', H-5''), 7.60 (s, 1H, H-2'), 8.29 (s, 1H, H-5). ¹³C NMR (DMSO-*d*₆) δ ppm: 18.499, 44.750, 112.463, 113.385, 123.238, 124.937, 127.818, 131.117, 131.460, 131.917, 135.064, 136.543, 141.801, 144.369, 150.175, 152.896, 182.751 (DMSO-*d*₆: 38.875–40.125). Anal. Calc. for C₁₉H₁₂BrCl₂N₃O₂ (%): C, 49.06; H, 2.60; Br, 17.18; Cl, 15.24; N, 9.03%. Found: C, 49.00; H, 2.41; Br+Cl, 32.51; N, 8.83%.

(4-Bromophenyl){4-[(3,4-dihydroisoquinolin-2(1H)-yl)methyl]-7-methylfuro[2,3-*c*]pyridin-2-yl)methanone (PD8).

Yield: 1.04 g (75%). Light beige crystals, m.p. 134–135 °C (EtOAc). ¹H NMR (DMSO-*d*₆): δ ppm 2.77–2.85 (m, 7H, CH₃, H-3', H-4'), 3.65 (s, 2H, CH₂), 3.97 (s, 1H, H-1'), 6.97 (s, 1H, H-3), 7.08–7.10 (m, 3H, H-5'–H-7'), 7.73 (d, *J* 8.1, 2H, H-2'', H-6''), 7.84–8.01 (m, 3H, H-8', H-3'', H-5''), 8.31 (s, 1H, H-5). ¹³C NMR (DMSO-*d*₆) δ ppm: 18.424, 28.709, 50.176, 55.260, 56.652, 114.820, 125.471, 125.977, 126.387, 126.503, 127.663, 128.439, 131.395, 131.870, 132.248, 133.998, 134.614, 135.185, 142.052, 412.872, 150.381, 152.291, 182.851 (DMSO-*d*₆: 38.878–40.128). Anal. Calc for C₂₅H₂₁BrN₂O₂ (%): C, 65.08; H, 4.59; Br, 17.32; N, 6.07%. Found: C, 65.01; H, 4.40; Br, 17.48; N, 6.03%.

4-[[2-(4-Bromobenzoyl)-7-methylfuro[2,3-*c*]pyridin-4-yl]methyl]piperazine-1-carbaldehyde hydrochloride (PD9).

Yield: 0.98 g (68%). Light beige crystals, m.p. 233–239 °C (EtOH). ¹H NMR (DMSO-*d*₆): δ ppm 2.91 (s, 3H, CH₃), 3.51 (s, 8H, H-2', H-3', H-5', H-6'), 4.74 (s, 2H, CH₂), 7.81 (d, *J* 8.5, 2H, H-2'', H-6''), 8.10–8.14 (m, 2H, H-3'', H-5''), 8.45 (s, 1H, H-3), 8.75 (s, 1H, CH), 10.09 (s, 1H, H-5). ¹³C NMR (DMSO-*d*₆) δ ppm: 18.309, 52.458, 53.228, 56.754, 58.447, 60.172, 114.820, 126.343, 127.612, 131.331, 131.838, 132.120, 135.191, 141.962, 142.661, 150.278, 152.189, 182.774 (DMSO-*d*₆: 38.878–40.122). Anal. Calc. for C₂₁H₂₁BrClN₃O₃ (%): C, 52.68; H, 4.42; Br, 16.69; Cl, 7.41; N, 8.78%. Found: C, 52.45; H, 4.29; Br+Cl, 24.21; N, 8.71%.

3-[4-[(2-(4-bromobenzoyl)-7-methylfuro[2,3-c]pyridin-4-yl)methyl]piperazin-1-yl]propanenitrile (**PD10**).

Yield: 1.18 g (84%). Light beige crystals, m.p. 129–132 °C (EtOH). ¹H NMR (DMSO-*d*₆): δ ppm 2.44–2.61 (m, 14H, CH₃, H-2', H-3', H-5', H-6', DMF), 2.75 (s, 4H, 2CH₂), 3.78 (s, 2H, CH₂), 7.80 (d, *J* 8.3, 2H, H-2'', H-6''), 7.86 (s, 1H, H-3), 8.01 (d, *J* 8.2, 2H, H-3'', H-5''), 8.23 (s, 1H, H-5). ¹³C NMR (DMSO-*d*₆) δ ppm: 14.877, 18.288, 52.117–52.220(d), 52.585, 56.554, 114.768, 119.833, 126.200, 127.585, 131.310, 131.817, 132.150, 135.164, 142.005, 142.672, 150.245, 152.175, 182.766 (DMSO-*d*₆: 38.832–40.082). Anal.Calc. for C₂₃H₂₃BrN₄O₂(%): C, 59.11; H, 4.96; Br, 17.10; N, 11.99%. Found: C, 59.03; H, 4.89; Br, 17.29; N, 11.72%.

(4-Bromophenyl)(7-methyl-4-[(pyridin-3-ylmethyl)amino]methyl)furo[2,3-c]pyridin-2-yl) methanone dihydrochloride (**PD11**).

Yield: 0.67 g (44%). Light beige crystals, m.p. 245–248 °C (EtOH). ¹H NMR (DMSO-*d*₆): δ ppm 2.93 (s, 3H, CH₃), 4.48 (s, 2H, CH₂), 4.66 (s, 2H, CH₂), 5.69 (br. s, 2H, 2NH⁺), 7.77–7.83 (m, 2H, H-2'', H-6''), 7.88 (s, 1H, H-3), 8.12–8.17 (m, 2H, H-3'', H-5''), 8.48 (s, 1H, H-5'), 8.74–8.82 (m, 3H, H-2', H-4', H-6'), 9.11 (s, 1H, H-5). ¹³C NMR (75 MHz, DMSO-*d*₆) δ 164.38 (C=O), 163.41 (2C), 143.04 (2C), 141.77 (2C), 141.14, 140.42, 139.64, 129.99 (3C), 126.22 (4C), 115.70, 111.85, 57.36 (CH₂-NH), 56.48 (NH-CH₂), 18.98 (CH₃). Anal.Calc. for C₂₂H₂₀BrCl₂N₃O₂(%): C, 51.89; H, 3.96; Br, 15.69; Cl, 13.92; N, 8.25%. Found: C, 51.73; H, 3.71; Br+Cl, 29.81; N, 8.04%.

(2,3-Dihydrobenzo[d][1,4]dioxin-6-yl)(4-[(3,4-dimethoxybenzyl)amino]methyl)-7-methylfuro pyridin-2-yl)methanone hydrochloride (**PD12**).

Yield: 0.94 g (61%). Light beige crystals, m.p. 208–211 °C (EtOH). ¹H NMR (DMSO-*d*₆): δ ppm 2.97 (s, 3H, CH₃), 3.77 (s, 3H, OCH₃), 3.80 (s, 3H, OCH₃), 4.16 (s, 2H, CH₂), 4.33–4.42 (m, 4H, H-2'', H-3''), 4.57 (s, 2H, CH₂), 5.69 (br. s, 1H, NH⁺), 6.86 (d, *J* 8.2, 1H, H-8''), 7.03–7.06 (m, 2H, H-5', H-6'), 7.63 (d, *J* 2.1, 1H, H-2'), 7.78 (dd, 8.5, *J* 2.2, 1H, H-7''), 8.32 (s, 1H, H-3), 8.82 (s, 1H, H-5''), 10.41 (s, 1H, H-5). ¹³C NMR (75 MHz, DMSO-*d*₆) δ 186.65 (C=O), 169.44 (C-C=O), 164.38, 162.00 (C-CH₃), 157.81, 142.07 (2C), 140.19 (2C), 127.65 (4C), 122.99 (4C), 105.07, 96.84, 95.57, 57.90 (CH₂-O-O-CH₂), 56.89 (CH₂-O-O-CH₂), 56.47 (4C), 18.99 (CH₃). Anal.Calc. for C₂₇H₂₇ClN₂O₆(%): C, 63.47; H, 5.33; Cl, 6.94; N, 5.48%. Found: C, 63.30; H, 5.16; Cl, 6.99; N, 5.33%.

(2,3-Dihydrobenzo[d][1,4]dioxin-6-yl)(7-methyl-4-[(4-(pyridin-3-ylmethyl)piperazin-1-yl)methyl]furo[2,3-c]pyridin-2-yl)methanone dihydrochloride (**PD13**).

Yield: 0.97 g (58%). Light beige crystals, m.p. 224–227 °C (EtOH). ¹H NMR (DMSO-*d*₆): δ ppm 2.96 (s, 3H, CH₃), 3.39–3.46 (m, 8H, H-2', H-3', H-5', H-6'), 4.33–4.43 (m, 6H, H-2'', H-3'', CH₂), 4.70 (m, 2H, CH₂), 5.48 (br. s, 2H, 2NH⁺), 7.00–7.10 (m, 2H, H-3, H-8''), 7.62 (d, *J* 2.1, 1H, H-5''), 7.76 (dd, 8.5, *J* 2.1, 1H, H-7''), 8.39 (s, 1H, H-5'''), 8.65 (s, 1H, H-4'''), 8.77 (s, 1H, H-2'''), 8.82 (d, *J* 5.2, H-6'''), 9.06 (s, 1H, H-5). ¹³C NMR (DMSO-*d*₆) δ ppm: 15.728, 47.653, 63.875, 64.645, 113.920, 117.511, 118.498, 124.179, 126.519, 128.545, 137.823, 143.107, 143.376, 144.678, 146.819, 148.987, 149.487, 155.700, 180.995 (DMSO-*d*₆: 38.741–39.997). Anal.Calc. for C₂₈H₃₀Cl₂N₄O₄(%): C, 60.33; H, 5.42; Cl, 12.72; N, 10.05%. Found: C, 60.16; H, 5.27; Cl, 12.87; N, 9.83%.

(2,3-Dihydrobenzo[d][1,4]dioxin-6-yl)(4-[(4-(2-hydroxyethyl)piperazin-1-yl)methyl]-7-methylfuro[2,3-c]pyridin-2-yl)methanone dihydrochloride (**PD14**).

Yield: 0.97 g (75%). Light beige crystals, m.p. 252–255 °C (EtOH). ¹H NMR (DMSO-*d*₆): δ ppm 3.00 (s, 3H, CH₃), 3.27 (t, *J* 4.9, 2H, CH₂), 3.62–3.71 (m, 8H, H-2', H-3', H-5', H-6'), 3.85 (t, *J* 5.0, 2H, CH₂), 4.34–4.42 (m, 4H, H-3'', H-8''), 4.82 (s, 2H, CH₂), 5.71 (br. s, 3H, OH, 2NH⁺), 7.04 (d, *J* 8.5, 1H, H-8''), 7.62 (d, *J* 2.1, 1H, H-5''), 7.78 (dd, *J* 8.5, 2.1, 1H, H-7''), 8.46 (s, 1H, H-3), 8.85 (1H, H-5). ¹³C NMR (400 MHz, DMSO-*d*₆) δ 15.89, 55.09, 63.87, 64.64, 113.98, 117.53, 118.49, 124.16, 128.60, 137.53, 143.26, 143.38, 148.97, 149.50, 155.52, 181.05. Anal.Calc. for C₂₄H₂₉Cl₂N₃O₅(%): C, 56.48; H, 5.73; Cl, 13.89; N, 8.23%. Found: C, 56.31; H, 5.61; Cl, 13.97; N, 8.10%.

3.3. Computational Studies

3.3.1. System Preparation

The three-dimensional structure of wild-type (PDB ID: 1M17) [52], L858R/T790M (PDB ID: 4I22) [53] and L858R/T790M/C797S EGFR (PDB ID: 6LUD) [52] were obtained from the Protein Data Bank. These crystal structures complexed with known drugs and subsequently known drugs were extracted. A series of 14 furo[2,3-c]pyridine derivatives was built using the Gaussview 09 program. All the ligands were optimized using the Gaussian 09 program (HF/6-31G*) and, subsequently, the protonation states of all ionizable amino acids were characterized using ChemAxon at pH 7.0. Molecular docking studies were performed using the GOLD program. The setting of the docking was studied using the following parameter as 10 Å with a sphere and 100 docking poses. The docking runs in each complex were sorted and selected based on GOLD fitness score. Then, the docking results were visualized for interaction using the UCSF Chimera package. The docked PDs/EGFRs with the highest GOLD fitness scores were chosen as the initial structures for performing MD simulations.

3.3.2. Molecular Dynamics Simulation and Free Energy Calculation Based on Solvated Interaction Energy (SIE) Method

The initial structures of PDs/EGFRs derived from molecular docking were carried out using pmemd CUDA in the AMBER 16 program [54] under periodic boundary conditions with the isobaric isothermal (NPT) ensemble in triplicate. The general AMBER force fields GAFF [55] and FF14SB [56] were applied for the ligand and protein, respectively. The partial charges of ligand were generated as follows: (i) the 3D structure of PD derivatives were optimized using the HF/6-31G* method [57] in the Gaussian09 program; (ii) the electrostatic potential (ESP) charge and restrained ESP (RESP) charge of the ligand were obtained by the AMBER16 program. All studied complexes were solvated by the TIP3P water model [58]. All missing hydrogen atoms of the protein and ligand were added by the LEaP module and subsequently minimized. The sodium ions were randomly neutralized in the simulated systems by Cl[−] counter ions. The added hydrogen atoms and water molecules were then minimized using 2500 steps of the steepest descents (SD), followed by 2500 steps of the conjugated gradient (CG), before starting the MD simulations. The SHAKE algorithm was used to fix all covalent bonds involving hydrogen atoms [59]. The systems were heated up to 310 K for 100 ps. Finally, the whole system was performed under the NPT ensemble (310 K, 1 atm) until reaching 100 ns. The root mean square deviation (RMSD) of each system was calculated using all-atom, and then the MD trajectories from the last 10-ns simulation were extracted for analysis in terms of total binding free energy (ΔG_{bind}) based on the solvated interaction energy (SIE) method. The potent PD derivatives with the lowest binding free energy were selected to determine EGFR inhibitory as well as anticancer activity. After finding the more potent PD derivative obtained from in silico screening and in vitro evaluation, the 500-ns MD simulation was performed. In addition, the per-residue decomposition free energy ($\Delta G_{\text{bind, residue}}$) calculations were carried out using the MMPBSA.py module in AMBER16 [60]. The CPPTRJ module was used to calculate intermolecular hydrogen bonding.

3.4. Biological Studies

3.4.1. EGFR Inhibitory ACTIVITY

The IC₅₀ values of the potent PD derivatives obtained from the SIE method were measured using the ADP-Glo™ kinase assay kit as previously reported [19]. Firstly, 8 µL of buffer (40 mM Tris-HCl pH 7.5, 20 mM MgCl₂, and 0.1 mg/mL bovine serum albumin) were added to a 384-well plate (Promega, solid white). Secondly, 5 µL of 1.25 ng/µL EGFRs enzyme (wild-type, L858R/T790M, and L858R/T790M/C797S EGFR) and 2 µL of 1 µM of compounds/known drugs were added separately to individual cell cultures, followed by 10 µL of a mixture of 5 µM ATP and 2.5 µM poly(glu-tyr), and were incubated for 1 h at room temperature. Thirdly, 5 µL of the ADP-Glo reagent was added and incubated for 40 min.

Finally, 10 µL of kinase detection reagent was added and incubated at room temperature for 30 min and was detected by measuring the luminescence using a microplate reader (Infinite M200 microplate reader, Tecan, Männedorf, Switzerland). A triplicate assay was performed on all potent **PD** derivatives and known drugs. The percentage relative inhibition (%) of potent compounds was measured compared to the control with no inhibitor as shown in Equation (1):

$$\% \text{Relative inhibition} = \frac{(\text{positive} - \text{negative}) - (\text{sample} - \text{negative})}{(\text{positive} - \text{negative})} \times 100. \quad (1)$$

3.4.2. Cell Viability Assay

The cytotoxicity activities of potent **PD** derivatives obtained from the SIE method against A549 and H1975, as well as Vero (which are adherent cells), were assessed using MTT (3-(4,5-dimethyl-2-thiazolyl)-2,5-diphenyl-2H-tetrazolium bromide) assays. The A549 and Vero cells were grown in complete DMEM medium whereas H1975 cells were grown in complete RPMI medium supplemented with 10% (*v/v*) FBS, 100 U/mL penicillin and 100 µg/mL streptomycin. All cells were routinely cultured at 37 °C in a 5% (*v/v*) CO₂, 95% (*v/v*) air humidified incubator. A549 (5 × 10³ cells per well), H1975 (5 × 10³ cells per well), and Vero (2 × 10³ cells per well) cells were seeded into 96-well plates and incubated overnight. After cell attachment, cells were replenished using fresh medium with 0.1% FBS containing various concentrations of potent **PD** derivatives and known drugs and then incubated at 37 °C for 72 h. After that, fresh medium containing MTT solution (5 mg/mL) was added and incubated at 37 °C. After 3 h, the formed formazan crystal was dissolved with 100 µL of dimethyl sulfoxide (DMSO). Finally, the absorbance of formazan solution was measured at a wavelength 570 nm using a microplate reader (Infinite M200 microplate reader, Tecan, Männedorf, Switzerland). The independent treatments were repeated in triplicate. The IC₅₀ determination of compounds was achieved using GraphPad Prism version 9.0.

4. Conclusions

In this work, a combination of *in silico* and *in vitro* studies were performed to screen for novel EGFR inhibitors that could inhibit both wild-type and mutant forms of EGFR. We found that potent compounds from virtual screening exhibited promising EGFR inhibitory activity. In particular, **PD13** showed strong inhibition of wild-type and L858R/T790M double mutant EGFR, while L858R/T790M/C797S showed moderate inhibition. In addition, the most potent **PD13** revealed high cytotoxicity against A549 and H1975. In 500-ns MD simulations, the model of **PD13** and known drugs/EGFRs was stable. The binding affinity of **PD13** complexed with wild-type and mutant forms of EGFR was significantly higher than that of known drugs (except for the L858R/T790M/C797S system), which was consistent with the hot-spot residues and EGFR inhibitory activity. The $\Delta G_{\text{bind}}^{\text{residue}}$ calculations revealed that M793 and S797 are the main residues in the hinge region for the binding of **PD13** with three EGFR strains via H-bond formations. In addition, the binding of all studied **PD** compounds is driven mainly by vdW interaction. Our results showed that **PD13** could potentially act as a promising non-mutant and mutant EGFR drug for cancer therapy.

Supplementary Materials: The following supporting information can be downloaded at: <https://www.mdpi.com/article/10.3390/molecules28073014/s1>, ¹H NMR Spectra of compounds **PD1–PD14**.

Author Contributions: A.G., K.C., V.K. and T.R.; methodology, K.C., T.R. and A.Z.; software, K.C., T.R. and A.P.; validation, D.T., A.Z., V.K., T.A., P.M., A.P., A.G., I.Y., K.C. and T.R.; formal analysis, D.T., A.Z., V.K., T.A., P.M., A.P., A.G., I.Y., K.C. and T.R.; investigation, D.T. and V.C., L.D.; data curation, D.T., A.G. and T.R.; writing—original draft preparation, D.T., A.Z., V.K., T.A., P.M., A.P., A.G., I.Y., K.C. and T.R.; writing—review and editing, D.T., A.Z., V.K., T.A., P.M., A.P., A.G., I.Y., K.C. and T.R.; visualization, D.T., A.Z., V.K., T.A., P.M., A.P., A.G., I.Y., K.C. and T.R.; supervision, P.M.,

A.G., K.C. and T.R.; funding acquisition, A.Z., K.C. and T.R. All authors have read and agreed to the published version of the manuscript.

Funding: This work has been supported by the Ministry of Science and Higher Education of the Russian Federation (Southern Federal University, 2022, project FENW-2023-0011), Fundamental Scientific Research of the State Academies of Sciences for 2022–2025 (grant no. 0710-2019-0044.), and the Thailand Science Research and Innovation Fund, Chulalongkorn University (HEA662300073).

Institutional Review Board Statement: Not applicable.

Informed Consent Statement: Not applicable.

Data Availability Statement: Not applicable.

Acknowledgments: D.T. thanks the 90th Anniversary of Chulalongkorn University (CU) Fund (Ratchadaphiseksomphot Endowment Fund, GCUGR1125642021M), and the Potential Development in Research for Graduate student Project, Faculty of Science, Chulalongkorn university.

Conflicts of Interest: The authors declare no conflict of interest.

Sample Availability: Samples of the compounds are available from the authors.

References

- Engel, J.; Richters, A.; Getlik, M.; Tomassi, S.; Keul, M.; Termathe, M.; Lategahn, J.; Becker, C.; Mayer-Wrangowski, S.; Grütter, C. Targeting drug resistance in EGFR with covalent inhibitors: A structure-based design approach. *J. Med. Chem.* **2015**, *58*, 6844–6863. [\[CrossRef\]](#)
- Peters, S.; Zimmermann, S.; Adjei, A.A. Oral epidermal growth factor receptor tyrosine kinase inhibitors for the treatment of non-small cell lung cancer: Comparative pharmacokinetics and drug–drug interactions. *Cancer Treat. Rev.* **2014**, *40*, 917–926. [\[CrossRef\]](#) [\[PubMed\]](#)
- Oda, K.; Matsuoka, Y.; Funahashi, A.; Kitano, H. A comprehensive pathway map of epidermal growth factor receptor signaling. *Mol. Syst. Biol.* **2005**, *1*, 2005.0010. [\[CrossRef\]](#) [\[PubMed\]](#)
- Yarden, Y.; Sliwkowski, M.X. Untangling the ErbB signalling network. *Nat. Rev. Mol. Cell Biol.* **2001**, *2*, 127–137. [\[CrossRef\]](#) [\[PubMed\]](#)
- Datta, S.R.; Dudek, H.; Tao, X.; Masters, S.; Fu, H.; Gotoh, Y.; Greenberg, M.E. Akt phosphorylation of BAD couples survival signals to the cell-intrinsic death machinery. *Cell* **1997**, *91*, 231–241. [\[CrossRef\]](#)
- Chen, P.; Xie, H.; Sekar, M.C.; Gupta, K.; Wells, A. Epidermal growth factor receptor-mediated cell motility: Phospholipase C activity is required, but mitogen-activated protein kinase activity is not sufficient for induced cell movement. *J. Cell Biol.* **1994**, *127*, 847–857. [\[CrossRef\]](#)
- Kharitonov, A.; Chen, Z.; Sures, I.; Wang, H.; Schilling, J.; Ullrich, A. A family of proteins that inhibit signalling through tyrosine kinase receptors. *Nature* **1997**, *386*, 181–186. [\[CrossRef\]](#)
- Sternberg, M.J.; Gullick, W.J. A sequence motif in the transmembrane region of growth factor receptors with tyrosine kinase activity mediates dimerization. *PEDS* **1990**, *3*, 245–248. [\[CrossRef\]](#) [\[PubMed\]](#)
- Zhang, H. Osimertinib making a breakthrough in lung cancer targeted therapy. *Onco Targets Ther.* **2016**, *9*, 5489. [\[CrossRef\]](#) [\[PubMed\]](#)
- Bethune, G.; Bethune, D.; Ridgway, N.; Xu, Z. Epidermal growth factor receptor (EGFR) in lung cancer: An overview and update. *J. Thorac. Dis.* **2010**, *2*, 48–51. [\[PubMed\]](#)
- Li, X.; Fan, X.-X.; Jiang, Z.-B.; Loo, W.T.; Yao, X.-J.; Leung, E.L.-H.; Chow, L.W.; Liu, L. Shikonin inhibits gefitinib-resistant non-small cell lung cancer by inhibiting TrxR and activating the EGFR proteasomal degradation pathway. *Pharmacol. Res.* **2017**, *115*, 45–55. [\[CrossRef\]](#)
- Normanno, N.; De Luca, A.; Bianco, C.; Strizzi, L.; Mancino, M.; Maiello, M.R.; Carotenuto, A.; De Feo, G.; Caponigro, F.; Salomon, D.S. Epidermal growth factor receptor (EGFR) signaling in cancer. *Gene* **2006**, *366*, 2–16. [\[CrossRef\]](#)
- Torre, L.A.; Bray, F.; Siegel, R.L.; Ferlay, J.; Lortet-Tieulent, J.; Jemal, A. Global cancer statistics, 2012. *CA Cancer J. Clin.* **2015**, *65*, 87–108. [\[CrossRef\]](#) [\[PubMed\]](#)
- Perez, E.A. The role of adjuvant monoclonal antibody therapy for breast cancer: Rationale and new studies. *Curr. Oncol. Rep.* **2001**, *3*, 516–522. [\[CrossRef\]](#) [\[PubMed\]](#)
- Wang, X.; Zhang, S.; MacLennan, G.T.; Eble, J.N.; Lopez-Beltran, A.; Yang, X.J.; Pan, C.-X.; Zhou, H.; Montironi, R.; Cheng, L. Epidermal growth factor receptor protein expression and gene amplification in small cell carcinoma of the urinary bladder. *Clin. Cancer Res.* **2007**, *13*, 953–957. [\[CrossRef\]](#)
- Shia, J.; Klimstra, D.S.; Li, A.R.; Qin, J.; Saltz, L.; Teruya-Feldstein, J.; Akram, M.; Chung, K.Y.; Yao, D.; Paty, P.B. Epidermal growth factor receptor expression and gene amplification in colorectal carcinoma: An immunohistochemical and chromogenic in situ hybridization study. *Mod. Pathol.* **2005**, *18*, 1350–1356. [\[CrossRef\]](#) [\[PubMed\]](#)

17. Shepherd, F.A.; Rodrigues Pereira, J.; Ciuleanu, T.; Tan, E.H.; Hirsh, V.; Thongprasert, S.; Campos, D.; Maoleekoonpiroj, S.; Smylie, M.; Martins, R. Erlotinib in previously treated non-small-cell lung cancer. *NEJM* **2005**, *353*, 123–132. [[CrossRef](#)] [[PubMed](#)]
18. Siegel, R.L.; Miller, K.D.; Jemal, A. Cancer statistics, 2015. *CA Cancer J. Clin.* **2015**, *65*, 5–29. [[CrossRef](#)] [[PubMed](#)]
19. Pérez-Soler, R.; Chachoua, A.; Hammond, L.A.; Rowinsky, E.K.; Huberman, M.; Karp, D.; Rigas, J.; Clark, G.M.; Santabárbara, P.; Bonomi, P. Determinants of tumor response and survival with erlotinib in patients with non-small-cell lung cancer. *J. Clin. Oncol.* **2004**, *22*, 3238–3247. [[CrossRef](#)]
20. Kris, M.G.; Natale, R.B.; Herbst, R.S.; Lynch Jr, T.J.; Prager, D.; Belani, C.P.; Schiller, J.H.; Kelly, K.; Spiridonidis, H.; Sandler, A. Efficacy of gefitinib, an inhibitor of the epidermal growth factor receptor tyrosine kinase, in symptomatic patients with non-small cell lung cancer: A randomized trial. *JAMA* **2003**, *290*, 2149–2158. [[CrossRef](#)]
21. Michalczyk, A.; Klüter, S.; Rode, H.B.; Simard, J.R.; Grütter, C.; Rabiller, M.; Rauh, D.; Fritsche, A.; Elfringhoff, A.S.; Fabian, J. Structural insights into how irreversible inhibitors can overcome drug resistance in EGFR. *Bioorg. Med. Chem.* **2008**, *16*, 3482–3488. [[CrossRef](#)] [[PubMed](#)]
22. Heuckmann, J.M.; Rauh, D.; Thomas, R.K. Epidermal growth factor receptor (EGFR) signaling and covalent EGFR inhibition in lung cancer. *J. Clin. Oncol. Off. J. Am. Soc. Clin. Oncol.* **2012**, *30*, 3417–3420. [[CrossRef](#)] [[PubMed](#)]
23. Kalgutkar, A.S.; Dalvie, D.K. Drug discovery for a new generation of covalent drugs. *Expert Opin. Drug Discov.* **2012**, *7*, 561–581. [[CrossRef](#)] [[PubMed](#)]
24. Copeland, R.A.; Pompliano, D.L.; Meek, T.D. Drug–target residence time and its implications for lead optimization. *Nat. Rev. Drug Discov.* **2006**, *5*, 730–739. [[CrossRef](#)] [[PubMed](#)]
25. Kwak, E.L.; Sordella, R.; Bell, D.W.; Godin-Heymann, N.; Okimoto, R.A.; Brannigan, B.W.; Harris, P.L.; Driscoll, D.R.; Fidias, P.; Lynch, T.J. Irreversible inhibitors of the EGF receptor may circumvent acquired resistance to gefitinib. *Proc. Natl. Acad. Sci. USA* **2005**, *102*, 7665–7670. [[CrossRef](#)] [[PubMed](#)]
26. Cross, D.A.; Ashton, S.E.; Ghiorghiu, S.; Eberlein, C.; Nebhan, C.A.; Spitzler, P.J.; Orme, J.P.; Finlay, M.R.; Ward, R.A.; Mellor, M.J.; et al. AZD9291, an irreversible EGFR TKI, overcomes T790M-mediated resistance to EGFR inhibitors in lung cancer. *Cancer Discov.* **2014**, *4*, 1046–1061. [[CrossRef](#)]
27. Lelais, G.; Epple, R.; Marsilje, T.H.; Long, Y.O.; McNeill, M.; Chen, B.; Lu, W.; Anumolu, J.; Badiger, S.; Bursulaya, B. Discovery of (R, E)-N-(7-Chloro-1-(1-[4-(dimethylamino) but-2-enoyl] azepan-3-yl)-1 H-benzo [d] imidazol-2-yl)-2-methylisonicotinamide (EGF816), a Novel, Potent, and WT Sparing Covalent Inhibitor of Oncogenic (L858R, ex19del) and Resistant (T790M) EGFR Mutants for the Treatment of EGFR Mutant Non-Small-Cell Lung Cancers. *J. Med. Chem.* **2016**, *59*, 6671–6689.
28. Zhou, W.; Ercan, D.; Chen, L.; Yun, C.H.; Li, D.; Capelletti, M.; Cortot, A.B.; Chirieac, L.; Jacob, R.E.; Padera, R.; et al. Novel mutant-selective EGFR kinase inhibitors against EGFR T790M. *Nature* **2009**, *462*, 1070–1074. [[CrossRef](#)]
29. Zhou, W.; Ercan, D.; Janne, P.A.; Gray, N.S. Discovery of selective irreversible inhibitors for EGFR-T790M. *Bioorg. Med. Chem. Lett.* **2011**, *21*, 638–643. [[CrossRef](#)]
30. Planken, S.; Behenna, D.C.; Nair, S.K.; Johnson, T.O.; Nagata, A.; Almaden, C.; Bailey, S.; Ballard, T.E.; Bernier, L.; Cheng, H.; et al. Discovery of n-((3 r, 4 r)-4-fluoro-1-(6-((3-methoxy-1-methyl-1 h-pyrazol-4-yl) amino)-9-methyl-9 h-purin-2-yl) pyrrolidine-3-yl) acrylamide (pf-06747775) through structure-based drug design: A high affinity irreversible inhibitor targeting oncogenic egfr mutants with selectivity over wild-type egfr. *J. Med. Chem.* **2017**, *60*, 3002–3019.
31. Eberlein, C.A.; Stetson, D.; Markovets, A.A.; Al-Kadhimi, K.J.; Lai, Z.; Fisher, P.R.; Meador, C.B.; Spitzler, P.; Ichihara, E.; Ross, S.J.; et al. Acquired Resistance to the Mutant-Selective EGFR Inhibitor AZD9291 Is Associated with Increased Dependence on RAS Signaling in Preclinical Models. *Cancer Res.* **2015**, *75*, 2489–2500. [[CrossRef](#)] [[PubMed](#)]
32. Hung, J.M.; Arabshahi, H.J.; Leung, E.; Keyniss, J.; Barker, D. Synthesis and cytotoxicity of thieno [2, 3-b] pyridine and furo [2, 3-b] pyridine derivatives. *Eur. J. Med. Chem.* **2014**, *86*, 420–437. [[CrossRef](#)] [[PubMed](#)]
33. Garamvölgyi, R.; Dobos, J.; Sipos, A.; Boros, S.; Illyés, E.; Baska, F.; Kékesi, L.; Szabadkai, I.; Szántai-Kis, C.; Kéri, G. Design and synthesis of new imidazo [1, 2-a] pyridine and imidazo [1, 2-a] pyrazine derivatives with antiproliferative activity against melanoma cells. *Eur. J. Med. Chem.* **2016**, *108*, 623–643. [[CrossRef](#)] [[PubMed](#)]
34. Ibrahim, M.M.; Al-Refai, M.; Azmi, M.N.; Osman, H.; Bakar, M.H.A.; Geyer, A. Synthesis, characterization and cytotoxicity of new nicotinonitriles and their furo [2, 3-b] pyridine derivatives. *JICS* **2019**, *16*, 715–722. [[CrossRef](#)]
35. Rai, S.K.; Singh, P.; Khanam, S.; Tewari, A.K. Polymorphic study and anti-inflammatory activity of a 3-cyano-2-pyridone based flexible model. *NJC* **2016**, *40*, 5577–5587. [[CrossRef](#)]
36. Dorsey, B.D.; McDonough, C.; McDaniel, S.L.; Levin, R.B.; Newton, C.L.; Hoffman, J.M.; Darke, P.L.; Zugay-Murphy, J.A.; Emini, E.A.; Schleif, W.A. Identification of MK-944a: A second clinical candidate from the hydroxylaminepentanamide isostere series of HIV protease inhibitors. *J. Med. Chem.* **2000**, *43*, 3386–3399. [[CrossRef](#)]
37. Agarwal, R.; Jha, K.K.; Munshi, P.; Adepally, U.; Singh, A.; Charyd, M.T.; Sen, S. Substituted furopyridinediones as novel inhibitors of α-glucosidase. *RSC Adv.* **2015**, *5*, 90374.
38. Salunke, D.B.; Yoo, E.; Shukla, N.M.; Balakrishna, R.; Malladi, S.S.; Serafin, K.J.; Day, V.W.; Wang, X.; David, S.A. Structure–activity relationships in human Toll-like receptor 8-active 2, 3-diamino-furo [2, 3-c] pyridines. *J. Med. Chem.* **2012**, *55*, 8137–8151. [[CrossRef](#)]
39. Zubenko, A.; Divaeva, L.; Morkovnik, A.; Fetisov, L.; Sochnev, V.; Kononenko, K.; Bodryakov, A.; Klimenko, A. Structural Modification of Pyridoxal. Synthesis and Evaluation of Anti-Infective Activity of New 4-Chloro- and 4-Alkyl (dialkyl) aminomethyl-2-hetaryl (hetaroyl) furo[2, 3-c] pyridines. *Russ. J. Gen. Chem.* **2020**, *90*, 2242–2247. [[CrossRef](#)]

40. Hei, Y.-Y.; Shen, Y.; Wang, J.; Zhang, H.; Zhao, H.-Y.; Xin, M.; Cao, Y.-X.; Li, Y.; Zhang, S.-Q. Synthesis and evaluation of 2, 9-disubstituted 8-phenylthio/phenylsulfinyl-9H-purine as new EGFR inhibitors. *Bioorg. Med. Chem.* **2018**, *26*, 2173–2185. [\[CrossRef\]](#)
41. Karnik, K.S.; Sarkate, A.P.; Tiwari, S.V.; Azad, R.; Burra, P.V.; Wakte, P.S. Computational and Synthetic approach with Biological Evaluation of Substituted Quinoline derivatives as small molecule L858R/T790M/C797S triple mutant EGFR inhibitors targeting resistance in Non-Small Cell Lung Cancer (NSCLC). *Bioorg. Chem.* **2021**, *107*, 104612. [\[CrossRef\]](#) [\[PubMed\]](#)
42. Shen, J.; Zhang, T.; Zhu, S.-J.; Sun, M.; Tong, L.; Lai, M.; Zhang, R.; Xu, W.; Wu, R.; Ding, J. Structure-based design of 5-methylpyrimidopyridone derivatives as new wild-type sparing inhibitors of the epidermal growth factor receptor triple mutant (EGFR L858R/T790M/C797S). *J. Med. Chem.* **2019**, *62*, 7302–7308. [\[CrossRef\]](#) [\[PubMed\]](#)
43. Rajith, B.; Chakraborty, C.; NagaSundaram, N.; Ali, S.K.; Zhu, H. Structural signature of the G719S-T790M double mutation in the EGFR kinase domain and its response to inhibitors. *Sci. Rep.* **2014**, *4*, 5868.
44. Martínez-Jiménez, F.; Overington, J.P.; Al-Lazikani, B.; Marti-Renom, M.A. Rational design of non-resistant targeted cancer therapies. *Sci. Rep.* **2017**, *7*, 46632. [\[CrossRef\]](#)
45. Stamos, J.; Sliwkowski, M.X.; Eigenbrot, C. Structure of the epidermal growth factor receptor kinase domain alone and in complex with a 4-anilinoquinazoline inhibitor. *J. Biol. Chem.* **2002**, *277*, 46265–46272. [\[CrossRef\]](#)
46. Sepay, N.; Mondal, R.; Al-Muhanna, M.K.; Saha, D. Identification of natural flavonoids as novel EGFR inhibitors using DFT, molecular docking, and molecular dynamics. *NJC* **2022**, *46*, 9735–9744. [\[CrossRef\]](#)
47. Zhang, R.; Chen, S.; Zhang, X.; Yu, R.; Wan, S.; Geng, M.; Jiang, T. Synthesis and evaluation of novel non-covalent binding quinazoline glycoside derivatives targeting the L858R and T790M variants of EGFR. *RSC Adv.* **2016**, *6*, 36857–36862. [\[CrossRef\]](#)
48. Lei, H.; Fan, S.; Zhang, H.; Liu, Y.-J.; Hei, Y.-Y.; Zhang, J.-J.; Zheng, A.-Q.; Xin, M.; Zhang, S.-Q. Discovery of novel 9-heterocyclyl substituted 9H-purines as L858R/T790M/C797S mutant EGFR tyrosine kinase inhibitors. *Eur. J. Med. Chem.* **2020**, *186*, 111888. [\[CrossRef\]](#)
49. Bello, M.; Saldaña-Rivero, L.; Correa-Basurto, J.; García, B.; Sánchez-Espinosa, V.A. Structural and energetic basis for the molecular recognition of dual synthetic vs. natural inhibitors of EGFR/HER2. *Int. J. Biol. Macromol.* **2018**, *111*, 569–586. [\[CrossRef\]](#)
50. Kou, S.-B.; Lin, Z.-Y.; Wang, B.-L.; Shi, J.-H.; Liu, Y.-X. Evaluation of the binding behavior of olmutinib (HM61713) with model transport protein: Insights from spectroscopic and molecular docking studies. *J. Mol. Struct.* **2021**, *1224*, 129024. [\[CrossRef\]](#)
51. Zhang, H.-X.; Xiong, H.-X.; Li, L.-W. Investigation on the protein-binding properties of icotinib by spectroscopic and molecular modeling method. *Spectrochim. Acta Part A Mol. Biomol. Spectrosc.* **2016**, *161*, 88–94. [\[CrossRef\]](#) [\[PubMed\]](#)
52. Kashima, K.; Kawauchi, H.; Tanimura, H.; Tachibana, Y.; Chiba, T.; Torizawa, T.; Sakamoto, H. CH7233163 overcomes osimertinib resistant EGFR-Del19/T790M/C797S mutation. *Mol. Cancer Ther.* **2020**, *19*, 2288–2297. [\[CrossRef\]](#)
53. Gajiwala, K.S.; Feng, J.; Ferre, R.; Ryan, K.; Brodsky, O.; Weinrich, S.; Kath, J.C.; Stewart, A. Insights into the aberrant activity of mutant EGFR kinase domain and drug recognition. *Structure* **2013**, *21*, 209–219. [\[CrossRef\]](#) [\[PubMed\]](#)
54. Gotz, A.W.; Williamson, M.J.; Xu, D.; Poole, D.; Le Grand, S.; Walker, R.C. Routine microsecond molecular dynamics simulations with AMBER on GPUs. 1. Generalized born. *J. Chem. Theory Comput.* **2012**, *8*, 1542–1555. [\[CrossRef\]](#) [\[PubMed\]](#)
55. Wang, J.; Wolf, R.M.; Caldwell, J.W.; Kollman, P.A.; Case, D.A. Development and testing of a general amber force field. *J. Comput. Chem.* **2004**, *25*, 1157–1174. [\[CrossRef\]](#)
56. Maier, J.A.; Martinez, C.; Kasavajhala, K.; Wickstrom, L.; Hauser, K.E.; Simmerling, C. ff14SB: Improving the accuracy of protein side chain and backbone parameters from ff99SB. *J. Chem. Theory Comput.* **2015**, *11*, 3696–3713. [\[CrossRef\]](#)
57. Frisch, A. *Gaussian 09w Reference*; Gaussian, Inc.: Wallingford, CT, USA, 2009; 25p.
58. Jorgensen, W.L.; Chandrasekhar, J.; Madura, J.D.; Impey, R.W.; Klein, M.L. Comparison of simple potential functions for simulating liquid water. *J. Chem. Phys.* **1983**, *79*, 926–935. [\[CrossRef\]](#)
59. Ryckaert, J.-P.; Ciccotti, G.; Berendsen, H.J. Numerical integration of the cartesian equations of motion of a system with constraints: Molecular dynamics of n-alkanes. *J. Comput. Phys.* **1977**, *23*, 327–341. [\[CrossRef\]](#)
60. Miller III, B.R.; McGee Jr, T.D.; Swails, J.M.; Homeyer, N.; Gohlke, H.; Roitberg, A.E. MMPBSA.py: An efficient program for end-state free energy calculations. *J. Chem. Theory Comput.* **2012**, *8*, 3314–3321. [\[CrossRef\]](#)

Disclaimer/Publisher's Note: The statements, opinions and data contained in all publications are solely those of the individual author(s) and contributor(s) and not of MDPI and/or the editor(s). MDPI and/or the editor(s) disclaim responsibility for any injury to people or property resulting from any ideas, methods, instructions or products referred to in the content.